


Gamma-band correlations in the primary visual cortexX. Liu ^{*}, P. Sanz-Leon, and P. A. Robinson*School of Physics, University of Sydney, Sydney, New South Wales 2006, Australia
and Center for Integrative Brain Function, University of Sydney, Sydney, New South Wales 2006, Australia* (Received 19 November 2018; revised manuscript received 25 November 2019; accepted 25 February 2020; published 14 April 2020)

This paper generalizes and extends previous work on using neural field theory to quantitatively analyze the two-dimensional (2D) spatiotemporal correlation properties of gamma-band (30–70 Hz) oscillations evoked by stimuli arriving at the primary visual cortex, and modulated by patchy connectivities that depend on orientation preference (OP). Correlation functions are derived analytically for general stimulus and measurement conditions. The theoretical results reproduce a range of published experimental results. These include (i) the existence of two-point oscillatory temporal cross correlations with zero time lag between neurons with similar OP; (ii) the influence of spatial separation of neurons on the strength of the correlations; and (iii) the effects of differing stimulus orientations. They go beyond prior work by incorporating experimentally observed patchy projection patterns to predict the 2D correlation structure including both OP and ocular dominance effects, thereby relaxing assumptions of translational invariance implicit in prior one-dimensional analysis.

DOI: [10.1103/PhysRevE.101.042406](https://doi.org/10.1103/PhysRevE.101.042406)**I. INTRODUCTION**

The primary visual cortex (V1) is the first cortical area to process visual inputs that arrive from the retina via the lateral geniculate nucleus (LGN) of the thalamus, and it feeds the processed signals forward to higher visual areas, and back to the LGN. The feed-forward visual pathway from the eyes to V1 is such that the neighboring cells in V1 respond to neighboring regions of the retina [1]. V1 can be approximated as a two-dimensional (2D) layered sheet [2]. Neurons that span vertically through multiple layers of V1 form a functional cortical column, and these neurons respond most strongly to a preferred stimulus orientation, right or left eye, direction of motion, and other feature preferences. Thus, various features of the visual inputs are mapped to V1 in different ways, and these maps are overlaid such that a single neural cell responds to several features. All feature preferences within a small subarea of the whole visual field are mapped to a fundamental region of V1, which is often termed as a hypercolumn [3–5].

A prominent feature of V1 is the presence of ocular dominance (OD) stripes, which reflect the fact that left- and right-eye inputs are mapped to alternating stripes ≈ 1 -mm wide, with each hypercolumn including left- and right-eye OD regions. Orientation preference (OP) of neurons for particular edge orientations in a visual field is determined by its receptive field properties, and it is mapped to regions within each hypercolumn such that neuron patches with particular OP are located adjacent to one another and OP spans the range from 0° to 180° . Typically, OP varies with azimuth relative to a center, or singularity, in the hypercolumn in an arrangement called a pinwheel. The OP angle in each pinwheel rotates either clockwise (negative pinwheel) or coun-

terclockwise (positive pinwheel), and neighboring pinwheels have opposite signs [6–11]. Hence, a hypercolumn must have left and right OD stripes with positive and negative pinwheels in each to cover the full set of the OP and OD preference, as suggested by Refs. [12,13]. In Figs. 1(a) and 1(b) we illustrate a negative pinwheel and a positive pinwheel, respectively, while Figs. 1(c) and 1(d) show a hypercolumn containing four pinwheels and a lattice of such hypercolumns, respectively. In such a lattice, the schematic resembles maps reconstructed from *in vivo* experiments, although the stripes have been approximated as straight here [6,14–16].

An additional feature of V1 is that groups of neurons with similar OP are preferentially linked within and between hypercolumns by patchy lateral connections [17,18]. Furthermore, patchy connections into and out of a given OP region are concentrated along an axis that points in the direction of the OP. This means that neurons that are sensitive to a contour of given orientation preferentially project to (and receive projections from) neurons of similar OP located along the continuation of that contour, which has been argued to be important to the completion of occluded contours and the binding problem [5,19–21]. Most notably, the projections from a given hypercolumn depend strongly on the OP at the source neurons within that hypercolumn and are thus strongly anisotropic [22].

When one considers neural activities in V1, numerous experiments and studies on multiunit activities (MUAs) and local field potentials (LFPs) in area 17 of cats [23–28] have shown that neurons with similar feature preference in V1 exhibit synchronized gamma-band (30–70-Hz) oscillations when the stimulus is optimal. They also showed that the corresponding two-point correlation functions of MUAs or LFPs commonly have peaks at zero time lag. Moreover, these synchronized gamma oscillations in V1 arise from the spatial structure of V1, modulated by the specific feature preferences

^{*}Corresponding author: xliu9362@uni.sydney.edu.au

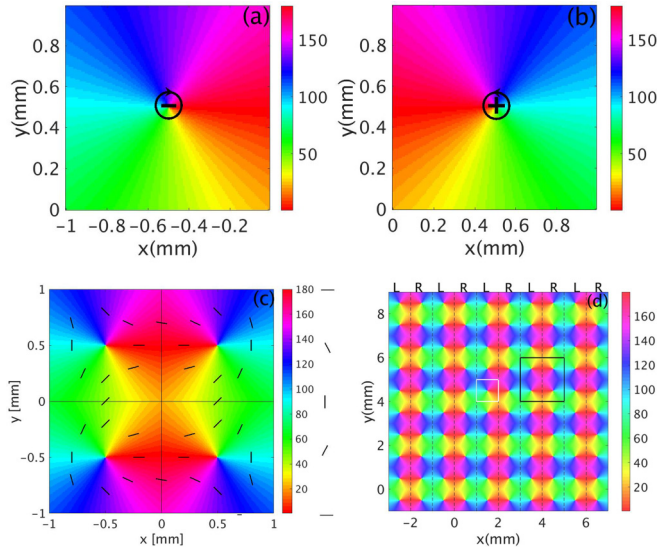


FIG. 1. Schematics of visual feature preference maps in V1 with color bars indicating OP in degrees. (a) Negative pinwheel. (b) Positive pinwheel. (c) Hypercolumn. The vertical line divides the hypercolumn into left and right OD columns of equal width, while the horizontal and vertical lines split the hypercolumn into four squares, each containing one OP pinwheel. The short bars highlight the OP at various locations. (d) Periodic spatial structure of OP and OD columns across a small piece of V1 comprising 25 hypercolumns. Dashed lines bound left (L) and right (R) OD columns. One pinwheel is outlined in white and one hypercolumn is outlined in black. Frames (a) and (b) are adapted from [29].

involved. It also has been argued that such synchronized oscillation in the gamma band may be involved in visual perception, the binding of related features into unified percepts, and the occurrence of visual hallucinations [30–34].

Several existing models have demonstrated nonlinear mechanisms for zero-lag synchronization in the brain, in terms of (i) signal relay via interrelated cortical areas for supporting the synchronization [35] and (ii) brain network modeling of entrainment, and how network properties such as recurrent inhibition, mutual inhibition, and gap junction coupling can affect the the zero-lag synchrony [36,37]. In addition, computational methods have been proposed to quantify the experimental data on zero-lag neuronal synchronization in the gamma band [38,39]. However, few studies have been conducted to quantitatively model the effects of the spatial structure and patchy connections of cortical neurons in the sensory cortices (we mainly focus on V1 in this paper) and to integrate them into a neural model of interacting neural populations to produce the spatiotemporal synchronized neural activities in the gamma frequency range. One exception is that Refs. [40–42] used neural field theory (NFT) with translationally invariant patchy propagation to show that patchy connectivity could support gamma oscillations with correlation properties the features of which resembled those of some of the above experiments. However, the effect of OP on the patchy propagators was not incorporated and the correlations were only explored as functions of one spatial dimension.

In this paper, we generalize and explore the spatiotemporal correlation functions of Refs. [41,42] to two spatial dimensions, and account for the effect of OP on the patchy propagators, which involves relaxing previous assumptions of translational invariance and incorporating the anisotropy of the overall envelope of patchy connectivity. We then compare the resulting spatiotemporal correlations with MUA experiments. In Sec. II, we briefly describe the relevant aspects of NFT including patchy propagators. In Sec. III, we derive the general 2D correlation function in V1 via the linear NFT transfer function of V1. Section IV describes a spatial propagator, which modulates the connection strength between cortical locations that have similar feature preference, and the Fourier coefficients of this propagator are applied to the numerical calculation of the correlation properties. The properties of these correlation functions are explored in Sec. V, including their predictions for oscillation frequency, time decay, effects of the spatial separation between the measurement points, and the modulation by the OP in V1. The predictions are compared with specific experimental outcomes in Sec. VI, and the results are summarized and discussed in Sec. VII.

II. THEORY

In order to analyze correlations in the patchily connected cortex, we first briefly review an established neural field model of the relevant corticothalamic system in Sec. II A, and calculation of its approximate transfer function in the gamma frequency range of several tens of hertz, with further details of the derivations available in prior papers [41,42]. In Secs. III and IV we generalize the patchy connectivity to two dimensions, including overall anisotropy of the envelope of patchy connections, due to OP effects, and calculate the resulting 2D correlation functions in order to treat the effects of both OD and OP together. Although this procedure is more involved than proposing an *ad hoc* theory that is restricted to gamma correlations, it links the analysis directly to the wider body of NFT results and the many constraints they have already placed on the parameters [40,41,43–49].

A. Neural field theory

NFT averages neural properties and activity over a linear scale of a few tenths of a millimeter to treat the dynamics on larger scales, which is appropriate for the present applications [43,46]. The previously developed corticothalamic NFT model [40] treats five neural populations, which are the long-range excitatory pyramidal neurons (e), midrange patchy excitatory neurons (m), short-range inhibitory interneurons (i), thalamic reticular neurons (r), and thalamic relay neurons (s); hence, it is termed the EMIRS model. Figure 2(a) shows the full EMIRS model and its connectivities between neural populations, including the axonal fields (described further below) ϕ_{ab} of spike rates arriving at neurons of population a from those of population b , where $a, b = e, m, i, r, s, n$. The external input signal ϕ_{sn} is incident on the relay nuclei.

In this paper, we are mainly concerned with cortical neural activities in the gamma band (30–70 Hz), which are higher than the resonant frequency (≈ 10 Hz) of the corticothalamic loops. This enables us to neglect the corticothalamic feedback

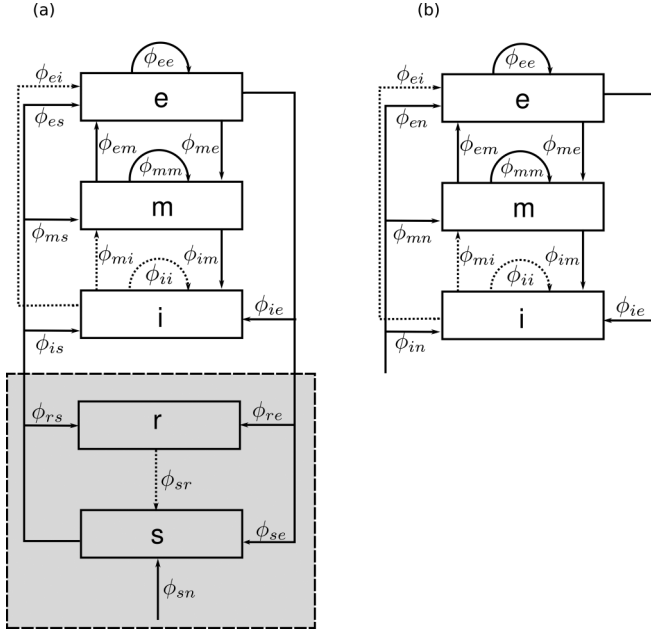


FIG. 2. Schematics of the corticothalamic system. (a) The full EMIRS model with the thalamus shown in the gray rectangle; each ϕ_{ab} quantifies the connection to population a from population b . (b) The simplified EMIRS model with the thalamic part approximated as a cortical input.

loops of the full EMIRS model, leading to the reduced model in Fig. 2(b). This model only includes the cortical excitatory, midrange, and short-range inhibitory populations, and the signals from the thalamus are treated as the input to the cortex. Thus, rather than having feedback inputs from the thalamus, we approximate these inputs as a common external input ϕ_{an} to the cortex. The subscript a denotes the three cortical neural populations (e, m, i).

Normal brain activity has been widely modeled as approximately corresponding to linear perturbations from a fixed point, with successful applications to experiments such as electroencephalographic (EEG) spectra, evoked response potentials, visual hallucinations, and other phenomena [33,44,45,50]. Hence, in the present paper, we restrict attention to the linear regime, which is justified so long as stimuli are not too strong.

Cells with voltage-gated ion channels produce action potentials when the soma potential exceeds a threshold θ_a . In the linear regime, changes Q_a in the mean population firing rate are related to the mean soma potential V_a by

$$Q_a(\mathbf{k}, \omega) = \rho_a V_a(\mathbf{k}, \omega), \quad (1)$$

where ρ_a is a constant. The mean linear perturbation V_a to the soma potential of neurons a is approximated by summing contributions V_{ab} resulting from activities of all types of synapses on neurons in the spatially extended population a from those of type b . Thus,

$$V_a(\mathbf{r}, t) = \sum_b V_{ab}(\mathbf{r}, t), \quad (2)$$

where \mathbf{r} is the spatial location on the cortex, approximated as a 2D sheet, and t is the time. In the Fourier domain, Eq. (2)

can be written as

$$V_a(\mathbf{k}, \omega) = \sum_b V_{ab}(\mathbf{k}, \omega), \quad (3)$$

where we define the Fourier transform and its inverse via

$$g(\mathbf{k}, \omega) = \int d^2\mathbf{r} \int dt g(\mathbf{r}, t) e^{i\omega t - i\mathbf{k}\cdot\mathbf{r}}, \quad (4)$$

$$g(\mathbf{r}, t) = \int \frac{d^2\mathbf{k}}{(2\pi)^2} \int \frac{d\omega}{(2\pi)} g(\mathbf{k}, \omega) e^{i\mathbf{k}\cdot\mathbf{r} - i\omega t}. \quad (5)$$

Due to the dependence of V_{ab} on the synaptic dynamics, signal dispersion in the dendrites, and soma charging, the soma potential corresponding to a delta function input can be approximated by

$$V_{ab}(\mathbf{k}, \omega) = L_{ab}(\omega) P_{ab}(\mathbf{k}, \omega), \quad (6)$$

where P_{ab} is the arrival rate of incoming spikes, and L_{ab} is the synapse-to-soma transfer function, with

$$L_{ab}(\omega) = (1 - i\omega/\alpha_{ab})^{-1} (1 - i\omega/\beta_{ab})^{-1}, \quad (7)$$

where α_{ab} and β_{ab} are the decay and rise rates of the soma response, respectively.

In Eq. (6), P_{ab} depends on Q_b at various source locations and earlier times [42], which influences ϕ_{ab} to propagate to a from b via axons, with

$$P_{ab}(\mathbf{k}, \omega) = \hat{v}_{ab}(\mathbf{k}, \omega) \phi_{ab}(\mathbf{k}, \omega), \quad (8)$$

$$\phi_{ab}(\mathbf{k}, \omega) = e^{i\omega\tau_{ab}} \Gamma_{ab}(\mathbf{k}, \omega) Q_b(\mathbf{k}, \omega), \quad (9)$$

where Γ_{ab} describes axonal propagation. In Eq. (9), τ_{ab} is the time delay between spatially discrete neuron populations (i.e., not between different \mathbf{r} values on the cortex) and \hat{v}_{ab} represents the coupling of ϕ_{ab} to population a . In the simplest case of proportional coupling,

$$\hat{v}_{ab}(\mathbf{k}, \omega) = N_{ab} s_{ab}, \quad (10)$$

where N_{ab} is the mean number of synaptic connections to each neuron of type a from neurons of type b and s_{ab} is their mean strength. More generally, \hat{v} can describe couplings that are sensitive to other features of ϕ_{ab} , such as spatial or temporal derivatives, which can increase sensitivity to features such as edges in the visual stimulus [40–42].

Axonal propagation can be approximately described by the damped wave equation [51–53]

$$\left[\frac{1}{\gamma_{ab}^2} \frac{\partial^2}{\partial t^2} + \frac{2}{\gamma_{ab}} \frac{\partial}{\partial t} + 1 - r_{ab}^2 \nabla^2 \right] \phi_{ab}(\mathbf{r}, t) = Q_b(\mathbf{r}, t), \quad (11)$$

where $\gamma_{ab} = v_{ab}/r_{ab}$ is the temporal damping coefficient, v_{ab} is the wave velocity, and r_{ab} is the characteristic range of axons that project to population a from b . In Fourier space, in the absence of patchy connections, one has [40]

$$\Gamma_{ab}^{(0)}(\mathbf{k}, \omega) = \frac{1}{(k^2 + q_{0ab}^2) r_{ab}^2}, \quad (12)$$

$$q_{0ab}^2 r_{ab}^2 = (1 - i\omega/\gamma_{ab})^2, \quad (13)$$

where k^2 denotes the scalar of $\mathbf{k} \cdot \mathbf{k}$. To incorporate the patchy propagation, we approximate the OP-OD structure of V1 as

being periodic, which results in periodic spatial modulation of the propagator in Eq. (9), giving [42]

$$\Gamma_{ab}(\mathbf{k}, \omega) = \sum_{\mathbf{K}} c_{\mathbf{K}} \Gamma_{ab}^{(0)}(\mathbf{k} - \mathbf{K}, \omega), \quad (14)$$

where the $c_{\mathbf{K}}$ are the Fourier coefficients of the function that describes the spatial feature preference (i.e., OP and/or OD), and \mathbf{K} ranges over the reciprocal lattice vectors of the periodic structure [42]. We analyze the $c_{\mathbf{K}}$ in Sec. IV below. It is worthwhile to note that $\Gamma_{ab}^{(0)}(\mathbf{k}, \omega)$ is translationally invariant; however, after including the spatial Fourier coefficients $c_{\mathbf{K}}$, $\Gamma_{ab}(\mathbf{k}, \omega)$ is only periodic but not translationally invariant because the orientation of the patchy projections changes with OP. We could think of Eq. (14) as the spatial Fourier transform of the product of $\Gamma_{ab}^{(0)}(\mathbf{r}, \omega)$ and a function $F(\mathbf{r}) = \sum_{\mathbf{K}'} c_{\mathbf{K}'} e^{i\mathbf{K}' \cdot \mathbf{r}}$ that describes the variation of the orientation of the projections with OP.

In order to perform further linear analysis of the system, we write $Q_a(\mathbf{k}, \omega)$ and $Q_b(\mathbf{k}, \omega)$ via Eqs. (2)–(8), which yields the set of linear equations

$$Q_a(\mathbf{k}, \omega) = \sum_b X_{ab}(\mathbf{k}, \omega) Q_b(\mathbf{k}, \omega), \quad (15)$$

with

$$X_{ab}(\mathbf{K}, \omega) = J_{ab}(\mathbf{k}, \omega) \Gamma_{ab}(\mathbf{k}, \omega), \quad (16)$$

$$J_{ab}(\mathbf{k}, \omega) = \rho_a L_{ab}(\omega) v_{ab}(\mathbf{k}, \omega) e^{i\omega \tau_{ab}}. \quad (17)$$

B. System transfer function and resonances

Turning to the system in Fig. 2, Eqs. (15)–(17) can be used to write the activity changes Q_e in the pyramidal neurons in terms of changes in the firing rate Q_n that implicitly drives the input signal ϕ_{sn} . At gamma frequencies, where corticothalamic feedback is too slow to respond effectively, this was found to yield [41,42]

$$T_{en}(\mathbf{k}, \omega) = \frac{Q_e(\mathbf{k}, \omega)}{Q_n(\mathbf{k}, \omega)} = \frac{X_{en}}{1 - X_{ee} - X_{em} - X_{ei}}. \quad (18)$$

Resonances of the system that determine spatiotemporal properties of the gamma oscillations arise from the poles of the transfer function, which correspond to zeros of the denominator of Eq. (18). At millimeter scales, $k \gg 1/r_{ee}$ and $|X_{ee}| \ll |X_{ei}|$, so the resonance condition becomes

$$1 - X_{em} - X_{ei} = 0. \quad (19)$$

Substituting Eqs. (7), (12), (16), and (17) into Eq. (19) gives

$$\begin{aligned} & \sum_{\mathbf{K}} \frac{\hat{G}(\mathbf{k}, \omega)}{(\mathbf{k} - \mathbf{K})^2 r_{em}^2 + (1 - i\omega/\gamma_{em})^2} \\ & = \left(1 - \frac{i\omega}{\alpha_{em}}\right) \left(1 - \frac{i\omega}{\beta_{em}}\right) - \frac{G_{ei}}{k^2 r_{ei}^2 + 1}, \end{aligned} \quad (20)$$

where

$$\hat{G}(\mathbf{k}, \omega) = c_{\mathbf{K}} \rho_e \hat{v}_{em}(\mathbf{k}, \omega). \quad (21)$$

When $\mathbf{k} \approx \mathbf{K}$, the denominator on the left hand side of Eq. (20) is small, and the corresponding term dominates the sum over the lattice vectors \mathbf{K} for the physiologically realistic

TABLE I. Nominal EMIRS model parameters from the literature [42,45].

Parameter	Variable	Value	Unit
Synaptodendritic rates	$\alpha_{em}, \alpha_{es}, \alpha_{ei}$	80	s^{-1}
	$\beta_{em}, \beta_{es}, \beta_{ei}$	800	s^{-1}
Projection range	r_{em}	2	mm
	r_{ei}	0.2	mm
	r_{es}	0.3	mm
Damping rates	γ_{em}	500	s^{-1}
	γ_{ei}	1500	s^{-1}
Gains	G_{es}	1.7	
	G_{em}	6.9	
	G_{ei}	-15.0	
dQ_e/dV_e	ρ_e	4200	$V^{-1} s^{-1}$

values of r_{em} and γ_{em} in Table I and ω . Although the sum formally does not converge, the smallest spatial scale of relevance (i.e., ≈ 0.1 mm) determines the maximum value of \mathbf{K} , which approximately equals to ten times the lowest reciprocal lattice vector, and it cuts off the sum at this maximum \mathbf{K} . Assuming $\hat{G}(\mathbf{k}, \omega)$ is purely spatial, $\hat{G}(\mathbf{k}, \omega)$ can be written as $\hat{G}(\mathbf{K})$, so Eq. (20) becomes [41,42]

$$\begin{aligned} & \frac{\hat{G}(\mathbf{K})}{(\mathbf{k} - \mathbf{K})^2 r_{em}^2 + (1 - i\omega/\gamma_{em})^2} \\ & = \left(1 - \frac{i\omega}{\alpha_{em}}\right) \left(1 - \frac{i\omega}{\beta_{em}}\right) - \frac{G_{ei}}{K^2 r_{ei}^2 + 1}, \quad (22) \\ \hat{G}(\mathbf{K}) & = \left[\left(1 - \frac{i\omega}{\alpha_{em}}\right) \left(1 - \frac{i\omega}{\beta_{em}}\right) - \frac{G_{ei}}{K^2 r_{ei}^2 + 1} \right] \\ & \times \left[(\mathbf{k} - \mathbf{K})^2 r_{em}^2 + \left(1 - \frac{i\omega}{\gamma_{em}}\right) \right]. \quad (23) \end{aligned}$$

Robinson [42] showed that if \hat{G} is sufficiently large and negative each value of \mathbf{K} can yield a resonance with frequency

$$\Omega^2 = \frac{\gamma[2\alpha\beta(1 - \hat{G}_{ei}) + \gamma(p^2 + 1)(\alpha + \beta)]}{2\gamma + \alpha + \beta}, \quad (24)$$

where the subscripts em on α , β , and γ are omitted, $p^2 = |\mathbf{k} - \mathbf{K}|^2$, and $\hat{G}_{ei} = G_{ei}/(K^2 r_{ei}^2 + 1)$. Each pair of \mathbf{K} and Ω gives a system resonance.

C. Transfer function due to resonances

The correlation analysis of [42] approximated the transfer function using only the lowest reciprocal lattice vector \mathbf{K} . We generalize that result to include higher order lattice vectors \mathbf{K}_j that describe finer spatial structure of the OP map, and denote the corresponding frequencies as Ω_j . Then, the transfer function is

$$T_{en}(\mathbf{k}, \omega) \approx \sum_{\mathbf{K}_j, \Omega_j} \frac{T_0(\mathbf{K}_j, \Omega_j)}{(\mathbf{k} - \mathbf{K}_j)^2 r_{em}^2 + q^2 r_{em}^2}, \quad (25)$$

$$T_0(\mathbf{k}, \omega) = \frac{J_{en} \hat{v}_{em} c_{\mathbf{K}}}{(1 - J_{ei})^2}, \quad (26)$$

$$q^2 r_{em}^2 = (1 - i\omega/\gamma_{em})^2 + \hat{v}_{em} c_{\mathbf{K}} / (1 - J_{ei}), \quad (27)$$

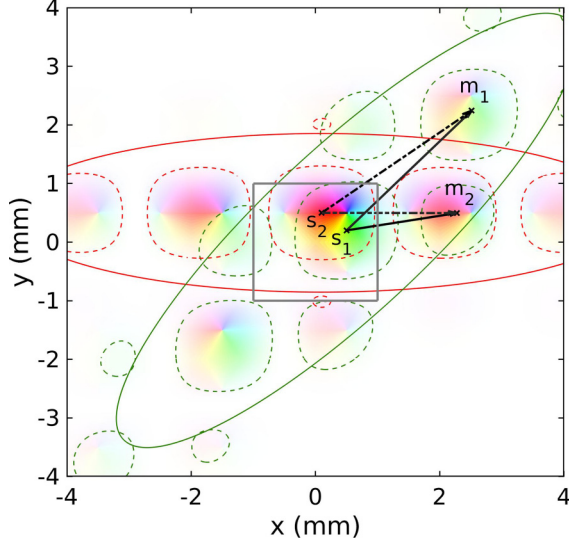


FIG. 3. Schematic for deriving the correlation functions, where \mathbf{s}_1 and \mathbf{s}_2 denote the stimulus or source points and \mathbf{m}_1 and \mathbf{m}_2 are the measurement points. The ellipses in solid green (red) lines indicate the overall shape of the orientation-modulated propagation from \mathbf{s}_1 (\mathbf{s}_2), as given by Eq. (43). The ellipsoids outlined in dotted green (red) lines indicate the patchiness of the propagation along the OP of \mathbf{s}_1 (\mathbf{s}_2), with period $k = 2\pi/a$. The solid and dash-dotted arrows denote propagation from \mathbf{s}_1 and \mathbf{s}_2 , respectively, to \mathbf{m}_1 and \mathbf{m}_2 .

where \hat{J}_{em} is defined in Eq. (17). Spatially Fourier transforming Eq. (25) then gives

$$T_{en}(\mathbf{r}, \omega) \approx \sum_{\mathbf{K}_j, \Omega_j} [(2\pi r_{em}^2)^{-1} e^{i\mathbf{K}_j \cdot \mathbf{r}} T_0(\mathbf{K}_j, \Omega_j) K_0(q|\mathbf{r}|)], \quad (28)$$

where K_0 is a modified Bessel function of the second kind [54].

III. CORRELATION FUNCTIONS

This section summarizes the use of transfer functions to derive the two-point correlation function between the cortical firing rates measured at two different locations when the cortex is stimulated at two locations, and generalizing the analysis of [42] and improving its notation.

We assume the visual cortex receives two temporally uncorrelated and spatially localized inputs at locations \mathbf{s}_1 and \mathbf{s}_2 . The spatial localization of inputs corresponds to the fact that the inputs are retinotopically mapped to V1 (i.e., the stimulus falls within the receptive fields of the V1 neurons at these two locations), while the lack of correlation is due to the facts that the input spike trains from LGN are uncorrelated with any features having the 25-ms periodicity of gamma and also that most experiments average over multiple trials, which is equivalent to random phase inputs (as opposed to the coherent-phase gamma response, which would only be strengthened by correlations in the inputs). Further, cortical activity is measured at \mathbf{m}_1 and \mathbf{m}_2 . Figure 3 shows a schematic of typical spatial locations and OPs involved in deriving the correlation function. The two ellipses in solid green and red centered at \mathbf{s}_1 and \mathbf{s}_2 represent anisotropic propagators

$G(\mathbf{r} - \mathbf{r}')$ for OPs $\phi(\mathbf{s}_1) = 45^\circ$ and $\phi(\mathbf{s}_2) = 0^\circ$. The arrows indicate propagation of neural activity from sources \mathbf{s}_j to measurement points \mathbf{m}_l .

We first derive equations for the neural activities at \mathbf{m}_1 and \mathbf{m}_2 due to inputs at \mathbf{s}_1 and \mathbf{s}_2 . The activity Φ at \mathbf{m}_l can be written as

$$\Phi(\mathbf{m}_l, t) = \sum_{j=1,2} \int d^2\mathbf{s}_j \int dt_j T_{en}(\mathbf{m}_l, \mathbf{s}_j, t - t_j) \Xi(\mathbf{s}_j, t_j), \quad (29)$$

where $T_{en}(\mathbf{m}_l, \mathbf{s}_j, t - t_j)$ is the transfer function that relates the activities at \mathbf{m}_l and time t to the stimulus Ξ at \mathbf{s}_j and time t_j .

Robinson [42] approximated a spatially localized input $\Xi(\mathbf{s}_j, \omega)$ as

$$\Xi(\mathbf{s}_j, \omega) = A_j(\omega) \delta(\mathbf{r} - \mathbf{s}_j) e^{i\psi(\mathbf{r}, \omega)}, \quad (30)$$

from which we obtain

$$\Xi(\mathbf{k}, \omega) = A_j(\omega) e^{-i\mathbf{k} \cdot \mathbf{s}_j} e^{i\psi(\mathbf{s}_j, \omega)}, \quad (31)$$

where the real quantities $A_j(\omega)$ and $\psi(\mathbf{s}_j, t_j)$ are the amplitude and the phase of the input at \mathbf{s}_j . We then find

$$\Phi(\mathbf{k}, \omega) = T_{en}(\mathbf{k}, \omega) \sum_{j=1,2} A_j(\omega) e^{-i\mathbf{k} \cdot \mathbf{s}_j} e^{i\psi(\mathbf{s}_j, \omega)}. \quad (32)$$

The two-point correlation function between \mathbf{m}_1 and \mathbf{m}_2 is [42]

$$C(\mathbf{m}_1, \mathbf{m}_2, \tau) = \langle \Phi_1(\mathbf{m}_1, t' + \tau) \Phi_2(\mathbf{m}_2, t') \rangle, \quad (33)$$

where $\tau = t - t'$, and the angle brackets refer to the averages over t' and over the phase of the inputs. A Fourier transform and integration over t' achieves the averaging [42] to yield

$$\begin{aligned} C(\mathbf{m}_1, \mathbf{m}_2, \tau) &= \int dt' \int \frac{d\omega}{2\pi} \int \frac{d\omega'}{2\pi} \int \frac{d^2\mathbf{k}}{(2\pi)^2} \int \frac{d^2\mathbf{k}'}{(2\pi)^2} \\ &\quad \times e^{-i\omega(t'+\tau) + i\omega't' + i\mathbf{k} \cdot \mathbf{m}_1 - i\mathbf{k}' \cdot \mathbf{m}_2} \\ &\quad \times \langle \Phi_1(\mathbf{k}, \omega) \Phi_2^*(\mathbf{k}', \omega') \rangle \\ &= \int \frac{d\omega}{2\pi} \int \frac{d^2\mathbf{k}}{(2\pi)^2} \int \frac{d^2\mathbf{k}'}{(2\pi)^2} \\ &\quad \times e^{-i\omega\tau + i\mathbf{k} \cdot \mathbf{m}_1 - i\mathbf{k}' \cdot \mathbf{m}_2} \langle \Phi_1(\mathbf{k}, \omega) \Phi_2^*(\mathbf{k}', \omega) \rangle. \end{aligned} \quad (34)$$

Substituting Eq. (32) into Eq. (35) and taking the inverse Fourier transform then gives

$$\begin{aligned} C(\mathbf{m}_1, \mathbf{m}_2, \tau) &= \left\langle \int \frac{d\omega}{2\pi} e^{-i\omega\tau} [T_{en}(\mathbf{m}_1 - \mathbf{s}_1, \omega) A_1(\omega) e^{i\psi(\mathbf{s}_1, \omega)} \right. \\ &\quad + T_{en}(\mathbf{m}_1 - \mathbf{s}_2, \omega) A_2(\omega) e^{i\psi(\mathbf{s}_2, \omega)}] \\ &\quad \times [T_{en}^*(\mathbf{m}_2 - \mathbf{s}_1, \omega) A_1(\omega) e^{-i\psi(\mathbf{s}_1, \omega)} \\ &\quad \left. + T_{en}^*(\mathbf{m}_2 - \mathbf{s}_2, \omega) A_2(\omega) e^{-i\psi(\mathbf{s}_2, \omega)}] \right\rangle, \end{aligned} \quad (36)$$

where the angle brackets now denote the average over the phases at \mathbf{s}_1 and \mathbf{s}_2 . If the phases of the inputs are random and uncorrelated,

$$\langle e^{i\psi(\mathbf{s}_1, \omega)} e^{i\psi(\mathbf{s}_2, \omega)} \rangle = \delta^2(\mathbf{s}_1 - \mathbf{s}_2), \quad (37)$$

so the cross terms between \mathbf{s}_1 and \mathbf{s}_2 in Eq. (36) are zero and

$$C(\mathbf{m}_1, \mathbf{m}_2, \tau) = \int \frac{d\omega}{2\pi} e^{-i\omega\tau} \{T_{en}(\mathbf{m}_1 - \mathbf{s}_1, \omega)T_{en}^*(\mathbf{m}_2 - \mathbf{s}_1, \omega)|A_1(\omega)|^2 + T_{en}(\mathbf{m}_1 - \mathbf{s}_2, \omega)T_{en}^*(\mathbf{m}_2 - \mathbf{s}_2, \omega)|A_2(\omega)|^2\}, \quad (38)$$

which is the sum of the correlations due to the two stimuli taken separately.

Finally, substituting Eq. (28) into Eq. (38), assuming inputs at different \mathbf{K}_j are uncorrelated, and letting $|A_1(\omega)| = |A_2(\omega)| = 1$ for simplicity gives

$$C(\mathbf{m}_1, \mathbf{m}_2, \tau) = (2\pi r_{em}^2)^{-1} \int \frac{d\omega}{2\pi} e^{-i\omega\tau} \times \sum_{\mathbf{K}_j, \Omega_j} \{ [e^{i\mathbf{K}_j \cdot (\mathbf{m}_1 - \mathbf{s}_1)} T_0(\mathbf{K}_j, \Omega_j) K_0(q|\mathbf{m}_1 - \mathbf{s}_1|)] \times [e^{i\mathbf{K}_j \cdot (\mathbf{m}_2 - \mathbf{s}_1)} T_0(\mathbf{K}_j, \Omega_j) K_0(q|\mathbf{m}_2 - \mathbf{s}_1|)]^* \} + \{ [e^{i\mathbf{K}_j \cdot (\mathbf{m}_1 - \mathbf{s}_2)} T_0(\mathbf{K}_j, \Omega_j) K_0(q|\mathbf{m}_1 - \mathbf{s}_2|)] \times [e^{i\mathbf{K}_j \cdot (\mathbf{m}_2 - \mathbf{s}_2)} T_0(\mathbf{K}_j, \Omega_j) K_0(q|\mathbf{m}_2 - \mathbf{s}_2|)]^* \}. \quad (39)$$

Some general aspects of Eq. (39) are that (i) the correlations depend on the separation of the measurement points and source points; (ii) the correlations fall off on a characteristic spatial scale of $(\text{Re}q)^{-1}$ because $K_0(z) \sim \exp(-z)$ at large z in the right half of the complex plane; and (iii) for the same reason there is an oscillation with spatial frequency $\text{Im}q$, while resonances in T_0 select dominant temporal frequencies in the correlations.

Having been derived systematically from corticothalamic NFT in the previous sections, Eq. (39) provides a systematic 2D generalization of the prior one-dimensional (1D) analysis [42]. Moreover, it links directly back to the wider applications of NFT, mentioned in the Introduction and Sec. II, many of which have constrained the model parameters, such as axonal ranges, neural time constants, and gains [40,41,44–49]. Equation (39) can also provide the starting point for approximation in terms of simpler mathematical functions, although we do not do so in the present paper.

IV. SPATIAL PATCHY PROPAGATOR IN TWO DIMENSIONS

Robinson [42] showed that the gamma response can be approximated as a sum of resonant responses at various \mathbf{K}_j . He further analyzed a spatially 1D system by approximating the contributions of these poles as Gaussians in $k - \omega$ space. This yielded patchy propagation with a Gaussian envelope as a function of distance, which explained a number of gamma correlation properties.

Here we generalize the analysis of Ref. [42] to the spatially 2D cortex to allow for the spatial anisotropy of the envelope of patchy connections, which extend further along a direction corresponding to the orientation of the source OP. We quantify the patchy propagation via the coefficients $c_{\mathbf{K}}$ in Eq. (14). Robinson [42] previously approximated the spatial propagator in one dimension as a Gaussian function. The propagation

was assumed to be isotropic with its patchiness described as $\cos(\mathbf{K}x)$, which is formed by a pair of complex conjugated coefficients $c_{+\mathbf{K}}$ and $c_{-\mathbf{K}}$, where \mathbf{K} is the lowest reciprocal lattice vector. However, in two dimensions, patches of neurons with similar feature preference are preferentially connected [17,55–57], with connections concentrated along an axis corresponding to their OP angle [22,58,59]. To model this overall modulation of the anisotropic propagation, we approximate the spatial propagator at each point and Fourier transform it to obtain a set of coefficients $c_{\mathbf{K}_j}$, where \mathbf{K}_j corresponds to the reciprocal lattice vectors. These coefficients $c_{\mathbf{K}_j}$ are used to calculate the transfer function T_{en} described by Eqs. (26) and (28).

A reasonable approximation to the envelope of the patchy connections that emerge from a particular point \mathbf{r}' is an elliptic Gaussian the long axis of which is oriented at the local OP ϕ at \mathbf{r}' . If $\mathbf{r}' = (x', y')$ and $\mathbf{r} = (x, y)$, we have

$$G(\mathbf{r} - \mathbf{r}') = \frac{1}{2\pi\sigma_x\sigma_y} \exp\left[-\frac{1}{2}\left(\frac{x_g^2}{\sigma_x^2} + \frac{y_g^2}{\sigma_y^2}\right)\right], \quad (40)$$

where

$$x_g = (x - x') \cos[\phi(x', y')] + (y - y') \sin[\phi(x', y')], \quad (41)$$

$$y_g = -(x - x') \sin[\phi(x', y')] + (y - y') \cos[\phi(x', y')], \quad (42)$$

where $\sigma_x = 2.6$ mm and $\sigma_y = 0.7$ mm are the spatial ranges along the preferred x_g and orthogonal y_g directions, with values chosen to match the experimental findings in a tree shrew by Ref. [22]. Figures 4(a) and 4(b) show contour plots of $G(\mathbf{r} - \mathbf{r}')$ for OPs of 0° and 45° , respectively, and source points \mathbf{r}' within a central hypercolumn [see Fig. 1(c)]; these effects of anisotropy break translational symmetry and cannot be treated in a 1D approximation.

Patchy propagation is modulated with spatial period $k = 2\pi/a$ parallel and orthogonal to OD columns, where $a \approx 2$ mm is the width of the hypercolumn. To incorporate this modulation, we multiply the oriented elliptic Gaussian function by a product of cosine functions that reflect this periodicity. This gives an approximate propagator profile of the form

$$G(\mathbf{r} - \mathbf{r}') = \frac{1}{2\pi\sigma_x\sigma_y} \exp\left[-\frac{1}{2}\left(\frac{x_g^2}{\sigma_x^2} + \frac{y_g^2}{\sigma_y^2}\right)\right] \times \{\cos[k_x(x - x')]\} + 1\} \{\cos[k_y(y - y')]\} + 1\}, \quad (43)$$

where $k_x = k_y = 2\pi/a$. We use this functional form to generalize the 1D cosine-modulated Gaussian form of Ref. [42] to represent the propagator of a given resonance in the 2D anisotropic case. This spatial patchy propagator is not translationally invariant and cannot be fully represented in one dimension due to the fact that the orientation of the patchy projections on the cortex changes with OP within each hypercolumn. But it is periodic with the period equals to the width of the hypercolumn. Figures 5(a) and 5(b) show the resulting propagators for $\phi(\mathbf{r}') = 0^\circ$ and 45° , with $\sigma_x = 2.6$ mm and $\sigma_y = 0.7$ mm. For both cases, when $\mathbf{r} - \mathbf{r}' < 0.5$ mm the underlying neurons respond to the stimulus, regardless of OP.

After performing a 2D Fourier transform on the propagators shown in Fig. 5, the coefficients $c_{\mathbf{K}_j}$ are illustrated in

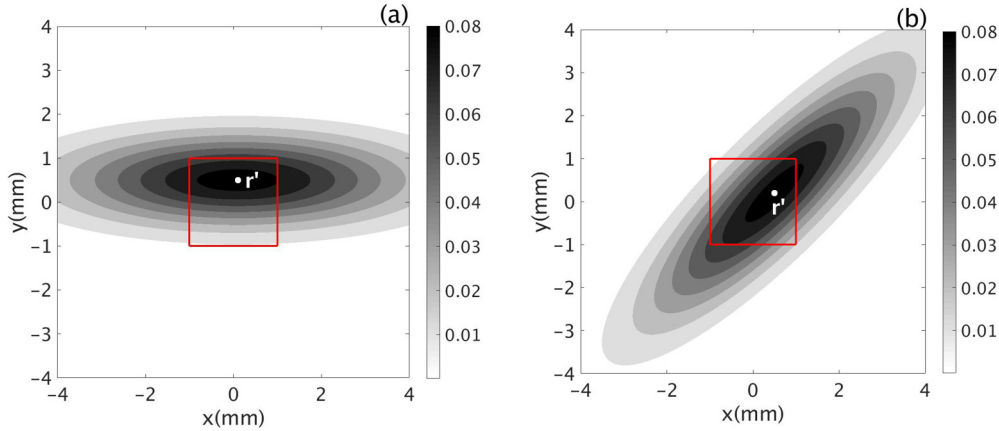


FIG. 4. Plots of Eq. (40) with the central hypercolumn outlined in red square; the color bar shows values of $G(\mathbf{r} - \mathbf{r}')$. (a) $OP = 0^\circ$. (b) $OP = 45^\circ$.

Fig. 6. Both sets of coefficients only have finite low frequency components. In the next section, we use a fraction of c_K , with lower K for evaluating the transfer function. The coefficients with lower K are enough to preserve the basic spatial propagation structure.

V. SPATIOTEMPORAL PROPERTIES OF THE CORRELATION FUNCTION

Here we first explore the temporal properties of the correlation function in Eq. (39); then we explore its spatial properties with a single input; lastly, we examine the spatial correlation in the case of two input sources. In all the cases described below, the correlation is calculated by numerically evaluating Eq. (39) and locating \mathbf{m}_1 , \mathbf{m}_2 , \mathbf{s}_1 , and \mathbf{s}_2 under different conditions. These conditions include using different optimal OPs for the measurement points and source points, and varying the distances between the measurement points. The results are presented in Fig. 7. All correlations are normalized such that $C(\mathbf{m}_1, \mathbf{m}_2, \tau) = 1$ when $\mathbf{s}_1 = \mathbf{s}_2$ and $\mathbf{m}_1 = \mathbf{m}_2$ are placed very close to the sources. Table I summarizes the parameters we use for the calculations. These parameters have been previously constrained by independent EEG-related experimental measurements, so they are not free [40,45].

A. Temporal correlation properties

In this section we explore the intrinsically 2D structure of gamma correlations predicted by our generalized model. In Fig. 7(a) we illustrate the temporal correlations evoked by binocular stimulation when \mathbf{s}_1 and \mathbf{s}_2 have the same OP $\phi(\mathbf{s}) = 90^\circ$ and \mathbf{s}_1 and \mathbf{s}_2 are located in the same hypercolumn but different OD columns. The strength of propagation of neural signals from two sources is indicated by contour lines of Eq. (43); the propagations are predominantly parallel to each other in this case. The measurement points \mathbf{m}_1 and \mathbf{m}_2 are located in a different hypercolumn to the source points but also have OPs of 90° ; they are approximately 2 mm away from each other and are located at approximately 2 mm from their respective collinear source points. We have also placed additional measurement points \mathbf{m}'_1 and \mathbf{m}'_2 , with the same OP as \mathbf{m}_1 and \mathbf{m}_2 , but approximately 4 mm from the sources.

Figure 7(b) shows the temporal correlation functions $C(\mathbf{m}_1, \mathbf{m}_2, \tau)$ and $C(\mathbf{m}'_1, \mathbf{m}'_2, \tau)$, where τ is the time lag between the measurement point and the source. Both oscillate at around 64 Hz, in the gamma range. Furthermore, each has a peak centered at $\tau = 0$, so the neural activities at \mathbf{m}_1 and \mathbf{m}_2 , \mathbf{m}'_1 and \mathbf{m}'_2 , are synchronized. The time for their envelopes to decrease to $1/e$ ($\sim 37\%$) of the peak value is ≈ 18 ms.

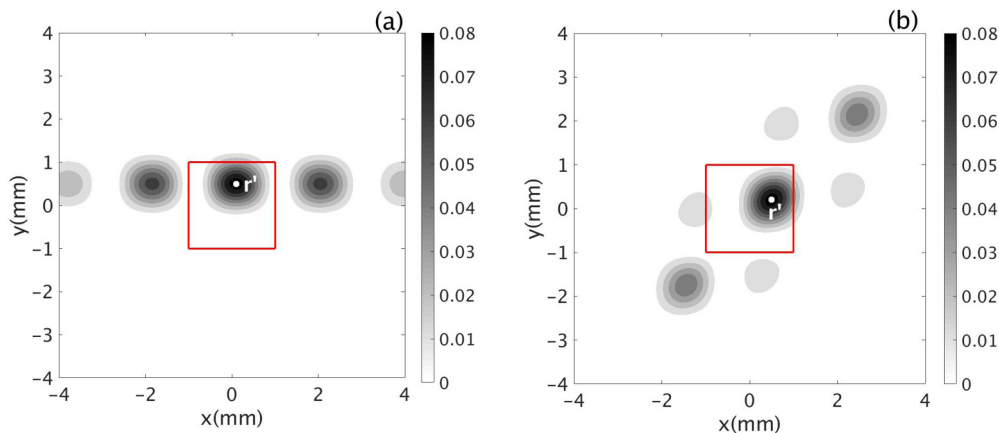


FIG. 5. Patchy propagator $G(\mathbf{r}, \mathbf{r}')$ in Eq. (43) with the central hypercolumn outlined in red square containing the source point \mathbf{r}' . The color bar shows the values of $G(\mathbf{r}, \mathbf{r}')$. (a) $\phi(\mathbf{r}') = 0^\circ$. (b) $\phi(\mathbf{r}') = 45^\circ$.

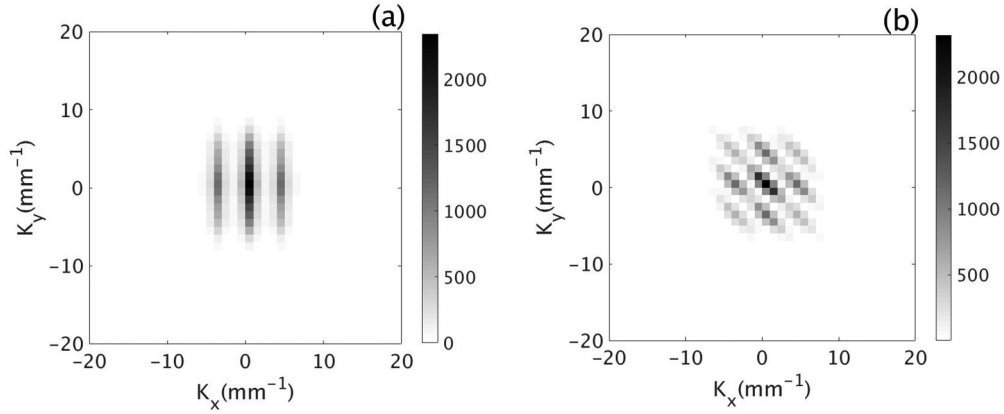


FIG. 6. Fourier coefficients of $G(\mathbf{r}, \mathbf{r}')$ in Eq. (43). Each pixel-like square represents one $c_{\mathbf{K}_j}$. The color bar shows the magnitudes of the coefficients. (a) $\phi(\mathbf{r}') = 0^\circ$. (b) $\phi(\mathbf{r}') = 45^\circ$.

However, when the measurement points are placed further away from the sources, the correlation at $\tau = 0$ becomes weaker, as seen by comparing the two curves.

Figure 7(c) shows a case for which the OP of all sources and measurement points is equal (at 45°). Figure 7(d) shows that the resulting correlation also has a central peak at zero time lag, oscillates in the gamma band at ≈ 55 Hz, and its envelope decreases by $1/e$ at $\tau \approx 21$ ms.

In order to explore the correlation properties between OD columns, we place all the source points and measurement points collinearly with OP = 0° in Fig. 7(e). Synchronized activities at \mathbf{m}_1 and \mathbf{m}_2 are shown by the center peak at $\tau = 0$ in Fig. 7(f). This correlation also exhibits gamma-band oscillation at ≈ 50 Hz, and the decrease by $1/e$ from the peak happens at ≈ 21 ms. One thing worth mentioning here is that the correlation strength due to intercolumnar connection shown in Fig. 7(f) is stronger than the intracolumnar connections in Fig. 7(b).

To further investigate the correlation properties, Fig. 7(g) shows a case in which the two measurement sites have orthogonal OPs, as do the sources: the OP at \mathbf{s}_1 and \mathbf{m}_1 is 90° , while at \mathbf{s}_2 and \mathbf{m}_2 it is 0° . The distance between the two measurement points is around 5.5 mm. In this case, \mathbf{s}_1 tends to evoke strong response at \mathbf{m}_1 , but not at \mathbf{m}_2 , which introduces an anticorrelation between \mathbf{m}_1 and \mathbf{m}_2 . Similarly, adding another source \mathbf{s}_2 only stimulates \mathbf{m}_2 and it again makes the activities at two measurement sites anticorrelated. This negative correlation is exactly shown by our predicted result in Fig. 7(h), which has a negative peak at $\tau = 0$.

B. Two-dimensional correlations due to a single source

To demonstrate how the correlation strength is influenced by the location of the measurement sites in two dimensions, their OP, and the resulting breaking of translational symmetry relative to prior 1D NFT analysis, we fix the location of a source \mathbf{s}_1 and a measurement point \mathbf{m}_1 , as in Fig. 7(a). We then map the correlation with the second measurement point \mathbf{m}_2 at $\tau = 0$ as a function of the latter's position on V1. The resulting 2D map is shown in Fig. 8, normalized to the maximum value of $C(\mathbf{m}_1, \mathbf{m}_2, 0)$.

Figure 8 shows a complex pattern the structure of which is closely tied to the joint OD-OP structure of V1 in two dimensions.

(i) The strongest positive correlations are located along a vertical axis passing through the source point \mathbf{s}_1 the OP of which is 90° .

(ii) Patterns of the correlated regions are almost symmetric around the vertical axis in (i).

(iii) The correlation strength falls off with distance between the two measurement points, as expected from Eq. (43). In addition, the correlation nearly vanishes when the measurement sites are greater than ≈ 7 mm apart (Fig. 8 only shows this in the positive y direction, but a similar result can be obtained in the negative y direction). This agrees with the experimental results, which suggested that significant oscillatory cross correlations are not observed when the spatial separation of neurons exceeds 7 mm.

(iv) The central peak shows that when the distance between \mathbf{m}_2 and \mathbf{s}_1 is less than 0.5 mm the correlations are strong and do not depend on the OPs at these locations, in accord with experiments [11,22].

(v) The positive correlations correspond to regions of OP approximately equal to the OP at \mathbf{s}_1 , while negative correlation regions correspond to OPs approximately perpendicular to the source OP angle. This shows that only neurons with similar OP to the source respond to the input stimulus.

C. Two-dimensional correlations due to two sources

Here we explore the dependence of the correlation function $C(\mathbf{m}_1, \mathbf{m}_2, 0)$ on the 2D position of measurement point \mathbf{m}_2 with two inputs \mathbf{s}_1 and \mathbf{s}_2 . The locations of the measurement points and source points are exactly as in the previous case and the additional source \mathbf{s}_2 has the same OP as \mathbf{s}_1 (i.e., 90°).

The resulting map shown in Fig. 9 exhibits similar properties to the previous case with one input, namely, the strongest correlations between the measurements points are along a vertical axis, which matches the OP of the sources. The positive correlation regions along this axis have a spatial period of 1 mm, corresponding to the minimum distance between regions having the same OP angle as the sources. However, the negative correlation regions now tend to align

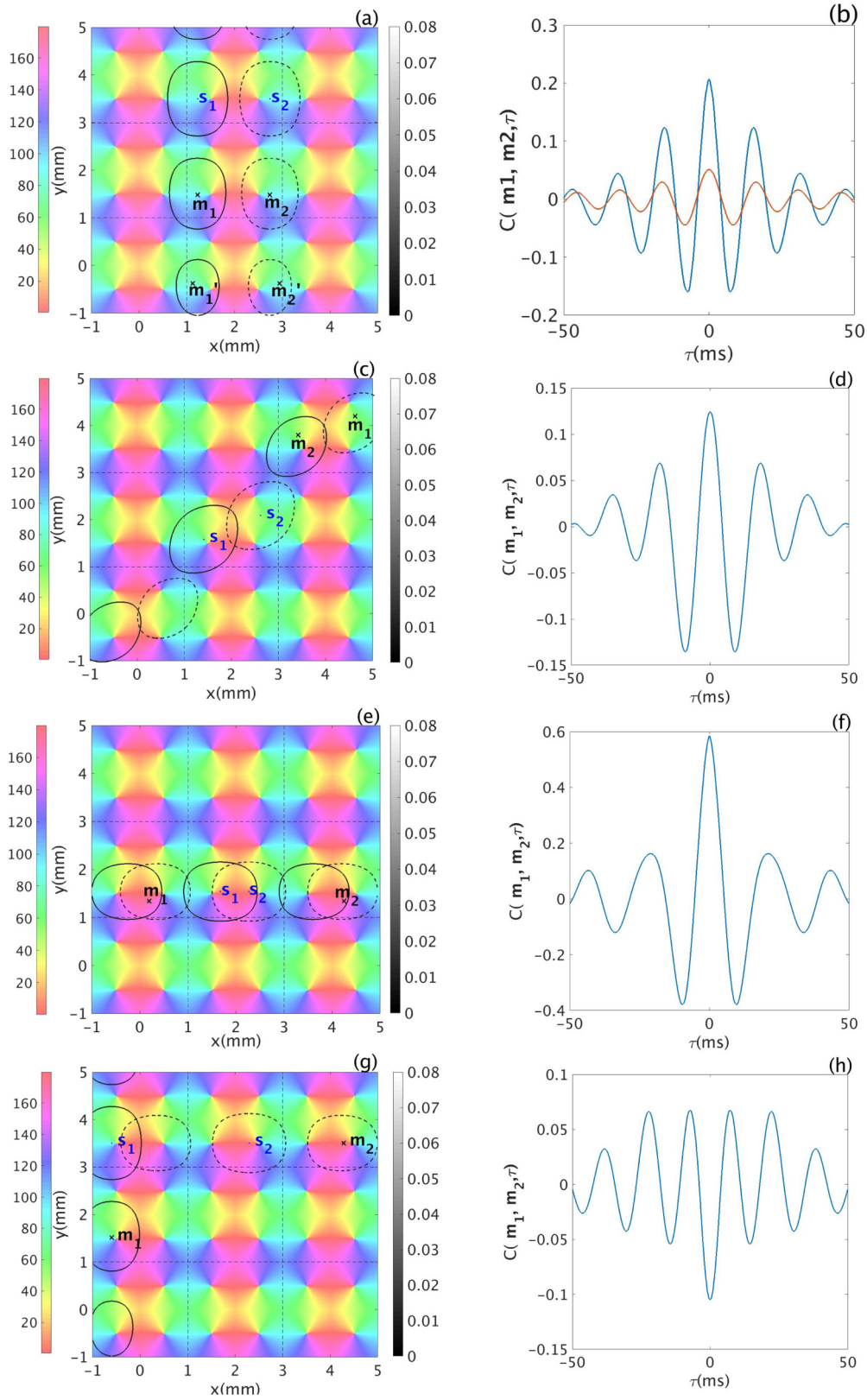


FIG. 7. Temporal correlations. (a) Locations of measurement points \mathbf{m}_1 and \mathbf{m}_2 , and source points s_1 , and s_2 within nine hypercolumns in V1. All points have OP of 90° . The left color bar shows the OP and the black circular contour lines scale at the right color bar; the strengths of propagators given by Eq. (43) are shown with solid and dashed contour lines for propagation from s_1 and s_2 , respectively. (b) Temporal correlations. The blue curve shows $C(\mathbf{m}_1, \mathbf{m}_2, \tau)$, while the orange curve shows $C(\mathbf{m}'_1, \mathbf{m}'_2, \tau)$. (c) As for (a) but with all points having OP of 45° . (d) Temporal correlation for (c). (e) As for (a) but with all points having OP of 0° . (f) Temporal correlation for (e). (g) As for (a) but with orthogonal OP of the sources. Furthermore, OP at s_1 is optimal for \mathbf{m}_1 whereas OP at s_2 is optimal for \mathbf{m}_2 . (h) Temporal correlation for (g).

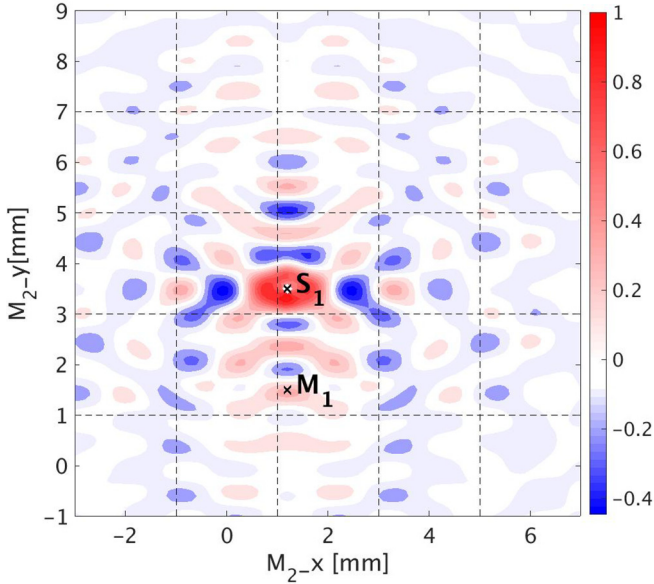


FIG. 8. Normalized contour plot of $C(\mathbf{m}_1, \mathbf{m}_2, 0)$ on V1, from Eq. (39) with a single input at \mathbf{s}_1 . The locations of \mathbf{s}_1 and measurement point \mathbf{m}_1 are fixed and the location of measurement point $\mathbf{m}_2(x, y)$ is given by the axes. The location and OP of \mathbf{s}_1 and \mathbf{m}_1 are the same as shown in Fig. 7(a). The color bar indicates the strength of the correlation. Dashed lines bound hypercolumns.

horizontally, which represents the direction orthogonal to the OP. The input source \mathbf{s}_2 is not surrounded by positive correlation regions as \mathbf{s}_1 is; rather, the negative correlations right above \mathbf{s}_2 correspond to a region where the OP of \mathbf{m}_2 is $\approx 0^\circ$. This is consistent with Sec. V A, where we showed that

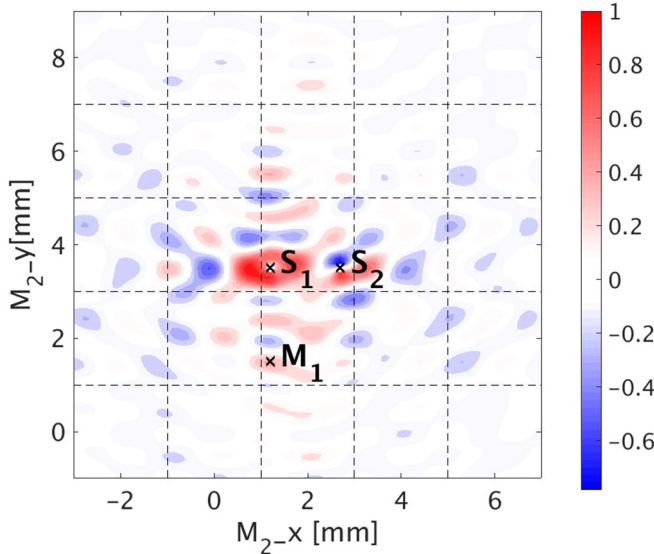


FIG. 9. Normalized contour plot of $C(\mathbf{m}_1, \mathbf{m}_2, 0)$ on V1, from Eq.(39) with two inputs \mathbf{s}_1 and \mathbf{s}_2 . The locations of the sources and measurement points \mathbf{m}_1 are fixed and the location of measurement point $\mathbf{m}_2(x, y)$ is given by the axes. The location and OP of \mathbf{s}_1 , \mathbf{s}_2 , and \mathbf{m}_1 are the same as shown in Fig. 7(a). The color bar indicates the strength of the correlation function. Dashed lines bound hypercolumns.

measurement points with orthogonal OPs tend to be anticorrelated at $\tau = 0$. In that case, we have predicted that when the OPs of two measurement points are 0° and 90° , respectively, the source that is optimal for one of the measurement sites introduces negative correlation between the two. Furthermore, these spatiotemporal patterns of the correlation strength also support a specific mechanism to encode the visual stimuli. For example, the specific constellation of activated neural patches (i.e., the red patches with positive correlation strength along the vertical axis) in Fig. 8 encodes the vertical orientation and collinearity of the visual object. This matches the hypothesis proposed in previous studies [25,28,60,61], which suggested that stimuli information is coded by the modulated neural synchronization strength.

VI. COMPARISON BETWEEN THEORY AND EXPERIMENT

In this section, we compare the predicted correlation functions with experimental correlations obtained from Engel *et al.* [24], who published temporal correlation functions of MUA and LFP data under various conditions, using the default parameters in Table I, unless otherwise stated. Our 2D analysis allows the joint OD-OP effects on gamma correlations to be treated for the first time, without restricting to one dimension with its implicit approximation of translational invariance of the patchy propagator. This set of initial tests is designed to demonstrate the applicability of the methods, and of Eq. (39) in particular, prior to future applications to a wider variety of experiments.

A. Description of the experiments

In these experiments, the MUA and LFP measurements were recorded from an array of electrodes that were inserted in five to seven spatially separated sites in area 17 of anesthetized adult cats, with neighboring recording sites spaced $400\text{--}500 \mu\text{m}$ apart. The locations of the receptive fields of all the measurement points were within 15° of the central area of the retina. Oriented light bars were used as binocular stimulation. Each trial lasted for 10 s and one trial set was composed of ten trials with identical stimuli. During each trial, the light bars were projected onto a screen that was placed 1.10 m in front of the eye plane of the cat, and the light bar was moved forward and backward across the receptive field during each trial. The autocorrelation function (ACF) and cross-correlation function (CCF) of the MUA data were computed. CCFs were calculated on each individual trial first, then averaged to get the final single CCF corresponding to a specific input stimulus [24].

B. Mapping experimental conditions to a regular lattice

In the present paper, we calculate the temporal correlation functions for two sets of experimental conditions, where the only difference between the two is the OP of the stimulus. One stimulus is oriented at 157° and another one oriented at 90° , as in the original experiments. We try to match to the experimental conditions as closely as possible by mapping the measurement points and stimulus onto our regularized grid

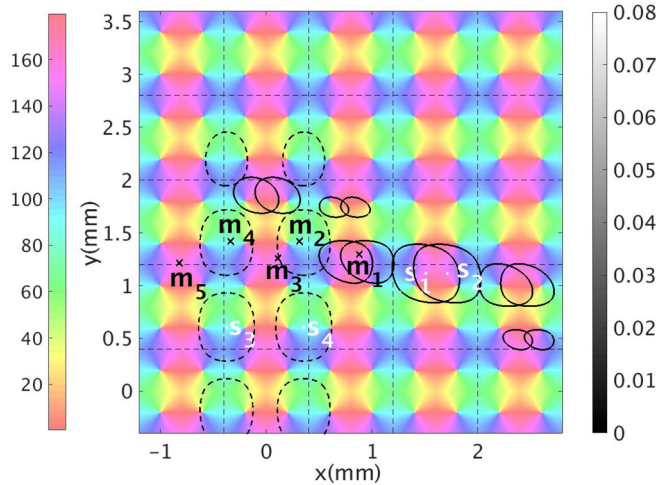


FIG. 10. Schematic of the two experimental conditions, showing measurement points \mathbf{m}_1 to \mathbf{m}_5 and source points on V1. The first experimental condition corresponds to a stimulus at 157° with corresponding sources denoted \mathbf{s}_1 and \mathbf{s}_2 , with solid black contour lines corresponding to the right color bar showing the propagation. The second experimental condition corresponds to a 90° stimulus. Here, \mathbf{s}_3 and \mathbf{s}_4 are the sources and dotted black contour lines corresponding to the right color bar showing the propagation strength. Dotted vertical and horizontal lines bound hypercolumns and the left color bar shows OP in degrees.

of hypercolumns in the following steps, and the mapping is shown in Fig. 10.

(i) In Engel *et al.*'s experiments [24], there were five fixed measurement points labeled as \mathbf{m}_1 to \mathbf{m}_5 , placed collinearly with a separation of $400 \mu\text{m}$ between adjacent points. Neurons at measurement points \mathbf{m}_1 , \mathbf{m}_3 , and \mathbf{m}_5 had similar orientation preference of 157° , while the OP of the cells at measurement points \mathbf{m}_2 and \mathbf{m}_4 was 90° . We first place \mathbf{m}_1 on the hypercolumn grid, at a location with OP of 157° . Then \mathbf{m}_3 and \mathbf{m}_5 are placed in adjacent hypercolumns with similar OPs. Finally, \mathbf{m}_2 is placed between \mathbf{m}_1 and \mathbf{m}_3 within a 90° OP region, while \mathbf{m}_4 is likewise placed between \mathbf{m}_3 and \mathbf{m}_5 . The fact that our grid of hypercolumns is regularized compared to the real OP map introduces slight distortions ($<0.5 \text{ mm}$) of the original cortical surface in order to preserve the measurement point OPs, so \mathbf{m}_1 to \mathbf{m}_5 are not exactly collinear. The OPs of \mathbf{m}_1 to \mathbf{m}_5 , computed after mapping onto our regular lattice, match the OPs given by the experiments to within 1° .

(ii) The experimental stimulation was binocular, so a single moving light bar at each point in time maps to source points on V1 (e.g., \mathbf{s}_1 and \mathbf{s}_2 , or \mathbf{s}_3 and \mathbf{s}_4), both with OP equal to the bar orientation, one located in the left OD column and one in the right OD column. The sources \mathbf{s}_1 and \mathbf{s}_2 indicate the 157° stimulus, and they have horizontal propagation of outgoing activities. In order to include \mathbf{m}_1 , \mathbf{m}_3 , and \mathbf{m}_5 within the propagation range from these sources, we choose to place these sources in the hypercolumn to the right of \mathbf{m}_1 and approximately in line with these measurement points; we could place the sources to the left of \mathbf{m}_5 , and produce similar results due to the symmetry of the grid. We do not put \mathbf{s}_1 and \mathbf{s}_2 in between the measurement points (e.g., in the hypercolumn under \mathbf{m}_3 in Fig. 10) because this would place \mathbf{m}_3 within

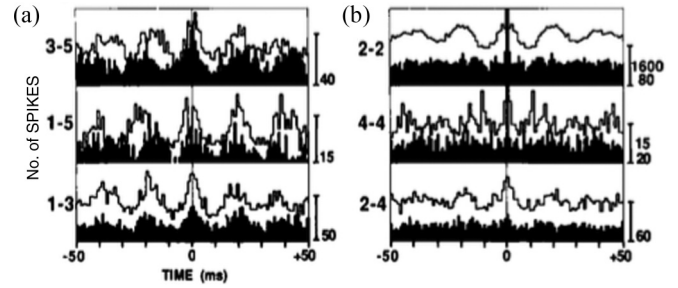


FIG. 11. Cross correlograms from experimental recordings calculated by [24]. In each case a baseline level of activity shifts the oscillatory part of the correlation upward and must be subtracted for comparison with the theoretical results. (a) Cross correlograms between measurement sites \mathbf{m}_3 and \mathbf{m}_5 , \mathbf{m}_1 and \mathbf{m}_5 , and \mathbf{m}_1 and \mathbf{m}_3 corresponding to an input light bar oriented at 157.5° . (b) Autocorrelograms of \mathbf{m}_2 and \mathbf{m}_4 in the top two rows, and cross correlograms on the bottom row between \mathbf{m}_2 and \mathbf{m}_4 , corresponding to the vertical light bar.

0.5 mm of the source, and would result in the neurons at \mathbf{m}_3 being activated regardless of its OP [22]. This would interfere with our aim of finding synchronized activities that are related to OP specific horizontal connections. The sources \mathbf{s}_3 and \mathbf{s}_4 represent the 90° stimulus, and have vertical propagation, so we place these sources in the hypercolumn below \mathbf{m}_2 and \mathbf{m}_4 (they could equally well be placed above). Their greater separation than \mathbf{s}_1 and \mathbf{s}_2 is due to the precise arrangement of different OPs within pinwheels.

(iii) Previous studies [62–64] found that the width of OD columns in cats is narrower than humans, and is around 0.4 mm . We use human OD column width ($\approx 1 \text{ mm}$) when modeling the hypercolumns grid, and hence we need to scale our grid down by a factor of 2.5 in Fig. 10 to match the experiments. We have also shortened the axon range of our neural field model (i.e., r_{em} , r_{ei} , and r_{es} in Table I) by the same factor during computation.

C. Comparison of predicted and experimental correlation functions

According to the experimental findings in Engel *et al.* [24], when the input light bar was oriented at 157.5° , measurement sites \mathbf{m}_1 , \mathbf{m}_3 , and \mathbf{m}_5 had synchronized oscillatory responses, and, when the input light bar was oriented at 90° , \mathbf{m}_2 and \mathbf{m}_4 were stimulated simultaneously. Figure 11 shows the CCFs and ACFs calculated from the experimental data, where the white (unfilled) correlograms correspond to forward movement of the stimulus, while the black (filled) correlograms correspond to the backward movements. In Fig. 11(a), the synchronized activities at \mathbf{m}_1 , \mathbf{m}_3 , and \mathbf{m}_5 were evoked by a 157.5° oriented stimulus. All the cross correlograms peak at zero time lag and have an average oscillation frequency of $\approx 54 \text{ Hz}$. The envelopes of the correlograms in the top and bottom rows of Fig. 11(a) decrease to $1/e$ of their central peak value at around 45 ms , with all levels measured relative to baseline activity; the 1-5 correlogram in the middle row is the only exception with a longer decay time (too long to estimate accurately from these data). The ACFs and CCF of \mathbf{m}_2 and \mathbf{m}_4 from a vertical light bar stimulus are shown in Fig. 11(b). The

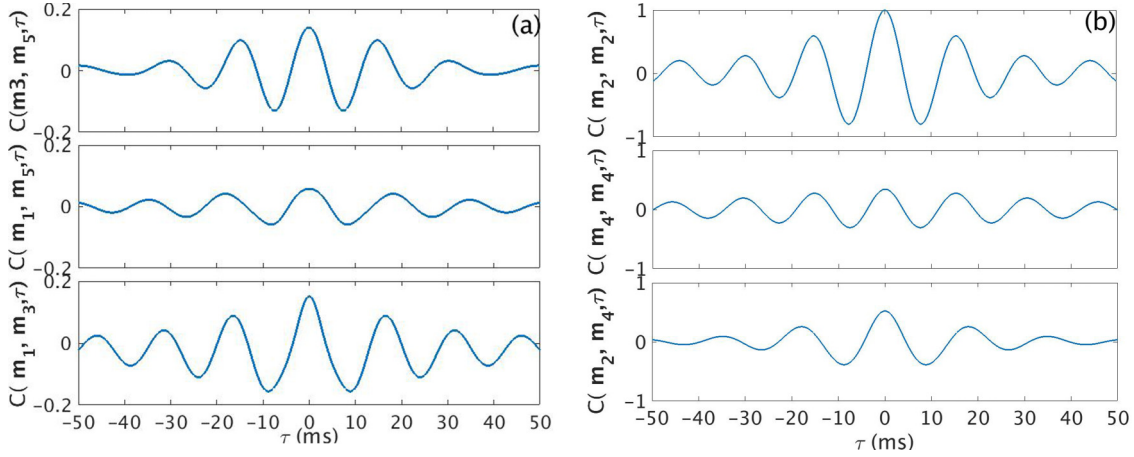


FIG. 12. Normalized temporal cross correlation with zero mean for experimental conditions with stimuli at 157.5° and 90° . (a) Normalized temporal correlation between measurement sites \mathbf{m}_3 and \mathbf{m}_5 , \mathbf{m}_1 and \mathbf{m}_5 , and \mathbf{m}_1 and \mathbf{m}_3 for a stimulus at 157.5° as illustrated in Fig. 10. (b) Normalized temporal cross correlation between \mathbf{m}_2 and \mathbf{m}_4 , and the autocorrelation function at \mathbf{m}_2 and \mathbf{m}_4 , for a stimulus at 90° .

CCF between \mathbf{m}_2 and \mathbf{m}_4 oscillates at around 55 Hz, and it takes more than 50 ms for the correlation strength to decrease to $1/e$ of its maximum.

Moreover, in the experiments it was also found that the correlation strength between \mathbf{m}_1 and \mathbf{m}_5 was weaker than that between \mathbf{m}_1 and \mathbf{m}_3 and between \mathbf{m}_3 and \mathbf{m}_5 [i.e., the bar that indicates the number of spikes, on the right of the plot in the second row of Fig. 11(a), has a smaller number than the other two plots]. This is due to the fact that the spatial distance between \mathbf{m}_1 and \mathbf{m}_5 is the largest, and the correlation strength falls off with distance.

We next explore the properties of our predicted correlation functions using Eq. (39) with the experimental conditions. Figure 12(a) shows the plots of our predicted temporal correlation functions between \mathbf{m}_3 and \mathbf{m}_5 , \mathbf{m}_1 and \mathbf{m}_5 , and \mathbf{m}_1 and \mathbf{m}_3 . As for the experimental CCFs, the theoretical CCFs (i) are oscillatory and peak at zero time lag, with the symmetry being due to the fact that both sources excite the same neural field of activity, so neither can lead nor lag the other, a feature shared with the 1D case [42]; (ii) have an oscillation frequency around 57 Hz that derives from the local neural resonance properties [41,42]; and (iii) have their characteristic time for the correlation envelope decrease to a factor of e of the maximum value at approximately 40 ms. These theoretical results agree with the experimental results, once a nonzero mean baseline is subtracted from the latter. Our results also capture the 2D spatial dependence of the maximum correlation strength and the effects of OP, which could only previously be treated qualitatively in 1D approximations. The plot in the middle row of Fig. 12(a) corresponds to the correlation between \mathbf{m}_1 and \mathbf{m}_5 and has the smallest amplitude of the three CCFs.

Figure 12(b) shows the predicted temporal correlation function generated by the vertical input light bar. In order to be consistent with the experimental results shown in Fig. 11(b), the autocorrelation functions of \mathbf{m}_2 and \mathbf{m}_4 are also included in the top two rows of Fig. 12(b). Both ACFs show oscillations in the gamma band. The CCF between \mathbf{m}_2 and \mathbf{m}_4 shows a center peak at $\tau = 0$ and oscillates at 55 Hz. The time for the envelope decay to $1/e$ of the center peak value is 25 ms. These

properties are also in accord with the experimental findings, including the intrinsically 2D effects due to OP variations.

VII. SUMMARY AND CONCLUSION

We have used 2D NFT of activity in the patchily connected primary visual cortex to generalize previously predicted spatiotemporal correlation functions to two dimensions in order to incorporate the joint 2D spatial structure of the OP map and OD columns of V1. Our results show that the neural activities are synchronized in the gamma band when neurons have similar feature preference. Features of the analysis and resulting predictions include the following.

(i) A 2D shape function has been included to modulate the experimentally observed spatial patchy propagation of neural signals preferentially along the OP direction. This models the propagation such that the mean propagation direction is aligned with the OP of the source, and the most strongly connected neurons are patchy and periodically located, while allowing weaker connections to nearby OPs that fall off according to a tuning curve consistent with experiment. The parameters of the shape function are chosen to match the propagation ranges and tuning curves observed in experiments [22].

(ii) The 2D two-point spatiotemporal correlation function has been systematically derived, enabling the correlation properties of arbitrary combinations of sources and measurement points to be predicted, including both OP and OD effects.

(iii) The properties of the generalized correlation function have been illustrated by numerical evaluation for various combinations of stimulation and measurement sites. The results demonstrate that synchronized gamma oscillation exists between paired groups of neurons that have similar OP to the sources. The correlation strength is predicted to be larger for intercolumnar connections than for intracolumnar ones, and to decrease as the measurement points move further away from the sources, becoming negligible for separations $\gtrsim 7$ mm. These features are intrinsically 2D and could not be obtained with prior 1D analyses.

(iv) Calculated 2D correlation maps show the changes expected in the peak correlation strength with respect to the variation of the OP of one of the measurement sites, and its distance to a second measurement site. Positive correlations appear as patches on an axis oriented at the OP of the source, and negative correlations occur where the OPs of the measurement sites are orthogonal to the OP of the source.

(v) Predicted temporal correlations have been compared with an initial set of experimental results from the literature. The results demonstrate that there is a close match between both in terms of the oscillation frequency and the characteristic decay time of the correlation function envelope. In addition, our CCFs capture the spatial dependence of correlation strength on distance between the measurement sites. As in one dimension a peak of correlation is observed at zero time lag for similar OP sources and measurement points because the neural activity drives spatially periodic modes—it is impossible for either of such locations to lead or lag the other; points with orthogonal OPs are found to be anticorrelated at zero time lag for analogous reasons, but with the mode having a peak at one point and a trough at the other. In the present paper, we can get a rough estimation of the correlations with the locations of the measurement and source points from a more realistic irregular OP map by substituting these locations into Eq. (39), but the results need to be validated in future works.

Overall, our generalized spatiotemporal correlation function reproduces the gamma-band oscillations observed in V1 and relates the spatially distributed neural responses to the

periodic spatial structure of OP and OD in V1. This paper lays the foundation to further investigate other visual perception phenomena such as the binding problem which focus on how different features of a visual object are integrated into a unified perception [65]. Furthermore, by following from a systematic NFT derivation, it immediately links the results to the wider body of successful NFT analyses of brain activity phenomena and the parameter constraints that they impose [40–49].

Our model can be further extended to correlation analysis of more realistic OP maps (e.g., OP maps developed from simulations or measured in experiments), and on other functional feature maps of V1; how strabismus or interocular rivalry affect gamma correlations; investigation of the dependences of gamma synchrony on attention, and how the neural synchronization relates to conscious perception; and study of abnormal neural synchronization on disorders. In addition, we could estimate model parameters and compare the model itself with alternatives by using dynamic causal modeling to maximize model evidence.

ACKNOWLEDGMENTS

This work was supported by the Australian Research Council under Laureate Fellowship Grant No. FL1401000025, Australian Research Council Centre of Excellence for Integrative Brain Function (ARC Grant No. CE140100007), and Discovery Project Grant No. DP170101778.

-
- [1] P. H. Schiller and E. J. Tehovnik, *Vision and the Visual System* (Oxford University, London, 2015).
- [2] M. J. Tovée, *An Introduction to the Visual System* (Cambridge University, Cambridge, England, 1996).
- [3] D. H. Hubel and T. N. Wiesel, Shape and arrangement of columns in cat's striate cortex, *J. Physiol.* **165**, 559 (1962).
- [4] D. H. Hubel and T. N. Wiesel, Sequence regularity and geometry of orientation columns in the monkey striate cortex, *J. Comp. Neurol.* **158**, 267 (1974).
- [5] R. Miikkulainen, J. A. Bednar, Y. Choe, and J. Sirosh, *Computational Maps in the Visual Cortex* (Springer, New York, 2005).
- [6] G. G. Blasdel, Orientation selectivity, preference, and continuity in monkey striate cortex, *J. Neurosci.* **12**, 3139 (1992).
- [7] V. Braitenberg and C. Braitenberg, Geometry of orientation columns in the visual cortex, *Biol. Cybern.* **33**, 179 (1979).
- [8] K. G. Götz, Do “d-blob” and “l-blob” hypercolumns tessellate the monkey visual cortex? *Biol. Cybern.* **56**, 107 (1987).
- [9] K. G. Götz, Cortical templates for the self-organization of orientation-specific d- and l-hypercolumns in monkeys and cats, *Biol. Cybern.* **58**, 213 (1988).
- [10] D. H. Hubel and T. N. Wiesel, Receptive fields, binocular interaction and functional architecture in the cat's visual cortex, *J. Physiol.* **160**, 106 (1962).
- [11] N. V. Swindale, The development of topography in the visual cortex: A review of models, *Network* **7**, 161 (1996).
- [12] P. C. Bressloff and J. D. Cowan, The visual cortex as a crystal, *Physica D* **173**, 226 (2002).
- [13] R. Veltz, P. Chossat, and O. Faugeras, On the effects on cortical spontaneous activity of the symmetries of the network of pinwheels in visual area V1, *J. Math. Neurosci.* **5**, 11 (2015).
- [14] T. Bonhoeffer and A. Grinvald, Iso-orientation domains in cat visual cortex are arranged in pinwheel-like patterns, *Nature (London)* **353**, 429 (1991).
- [15] T. Bonhoeffer and A. Grinvald, The layout of iso-orientation domains in area 18 of cat visual cortex: Optical imaging reveals a pinwheel-like organization, *J. Neurosci.* **13**, 4157 (1993).
- [16] K. Obermayer and G. G. Blasdel, Geometry of orientation and ocular dominance columns in monkey striate cortex, *J. Neurosci.* **13**, 4114 (1993).
- [17] C. D. Gilbert and T. N. Wiesel, Clustered intrinsic connections in cat visual cortex, *J. Neurosci.* **3**, 1116 (1983).
- [18] K. S. Rockland and J. S. Lund, Widespread periodic intrinsic connections in the tree shrew visual cortex, *Science* **215**, 1532 (1982).
- [19] Z. Li, A neural model of contour integration in the primary visual cortex, *Neural Comput.* **10**, 903 (1998).
- [20] G. Loffler, Perception of contours and shapes: Low and intermediate stage mechanisms, *Vision Res.* **48**, 2106 (2008).
- [21] M. Stemmler, M. Usher, and E. Niebur, Lateral interactions in primary visual cortex: A model bridging physiology and psychophysics, *Science* **269**, 1877 (1995).

- [22] W. H. Bosking, Y. Zhang, B. Schofield, and D. Fitzpatrick, Orientation selectivity and the arrangement of horizontal connections in tree shrew striate cortex, *J. Neurosci.* **17**, 2112 (1997).
- [23] R. Eckhorn, R. Bauer, W. Jordan, M. Brosch, W. Kruse, M. Munk, and H. J. Reitboeck, Coherent oscillations: A mechanism of feature linking in the visual cortex? *Biol. Cybern.* **60**, 121 (1988).
- [24] A. K. Engel, P. König, C. M. Gray, and W. Singer, Stimulus-dependent neuronal oscillations in cat visual cortex: inter-columnar interaction as determined by cross-correlation analysis, *Eur. J. Neurosci.* **2**, 588 (1990).
- [25] C. M. Gray, A. K. Engel, P. König, and W. Singer, Oscillatory responses in cat visual cortex exhibit inter-columnar synchronization which reflects global stimulus properties, *Nature (London)* **338**, 334 (1989).
- [26] Y. Hata, T. Tsumoto, H. Sato, and H. Tamura, Horizontal interactions between visual cortical neurones studied by cross-correlation analysis in the cat, *J. Physiol.* **441**, 593 (1991).
- [27] P. König, A. K. Engel, and W. Singer, Relation between oscillatory activity and long-range synchronization in cat visual cortex, *Proc. Natl. Acad. Sci. USA* **92**, 290 (1995).
- [28] W. Singer and C. M. Gray, Visual feature integration and the temporal correlation hypothesis, *Annu. Rev. Neurosci.* **18**, 555 (1995).
- [29] K. Kukjin, S. Michael, and S. Haim, Mexican hats and pin-wheels in visual cortex, *Proc. Natl. Acad. Sci. USA* **100**, 2848 (2003).
- [30] P. C. Bressloff, J. D. Cowan, M. Golubitsky, P. J. Thomas, and M. C. Wiener, What geometric visual hallucinations tell us about the visual cortex, *Neural Comput.* **14**, 473 (2002).
- [31] A. K. Engel, P. Fries, and W. Singer, Dynamic predictions: Oscillations and synchrony in top-down processing, *Nat. Rev. Neurosci.* **2**, 704 (2001).
- [32] C. M. Gray, A. K. Engel, P. König, and W. Singer, Stimulus-dependent neuronal oscillations in cat visual cortex: Receptive field properties and feature dependence, *Eur. J. Neurosci.* **2**, 607 (1990).
- [33] H. Henke, P. A. Robinson, P. M. Drysdale, and P. N. Loxley, Spatiotemporally varying visual hallucinations. I. Corticothalamic theory, *J. Theor. Biol.* **357**, 200 (2014).
- [34] M. Siegel, A. K. Engel, and T. H. Donner, Cortical network dynamics of perceptual decision-making in the human brain, *Front Hum. Neurosci.* **5**, 21 (2011).
- [35] D. Chawla, K. J. Friston, and E. D. Lumer, Zero-lag synchronous dynamics in triplets of interconnected cortical areas, *Neural Network* **14**, 727 (2001).
- [36] D. Huang and G. Pipa, Achieving synchronization of networks by an auxiliary hub, *Europhys. Lett.* **77**, 50010 (2007).
- [37] N. Kopell, G. B. Ermentrout, M. A. Whittington, and R. D. Traub, Gamma rhythms and beta rhythms have different synchronization properties, *Proc. Natl. Acad. Sci. USA* **97**, 1867 (2000).
- [38] P. König, A method for the quantification of synchrony and oscillatory properties of neuronal activity, *J. Neurosci. Methods* **54**, 31 (1994).
- [39] G. Pipa, D. W. Wheeler, W. Singer, and D. Nikolić, Neuroxidence: Reliable and efficient analysis of an excess or deficiency of joint-spike events, *J. Comput. Neurosci.* **25**, 64 (2008).
- [40] P. A. Robinson, Propagator theory of brain dynamics, *Phys. Rev. E* **72**, 011904 (2005).
- [41] P. A. Robinson, Patchy propagators, brain dynamics, and the generation of spatially structured gamma oscillations, *Phys. Rev. E* **73**, 041904 (2006).
- [42] P. A. Robinson, Visual gamma oscillations: Waves, correlations, and other phenomena, including comparison with experimental data, *Biol. Cybern.* **97**, 317 (2007).
- [43] G. Deco, V. K. Jirsa, P. A. Robinson, M. Breakspear, and K. Friston, The dynamic brain: From spiking neurons to neural masses and cortical fields, *PLoS Comput. Biol.* **4**, e1000092 (2008).
- [44] P. A. Robinson, C. J. Rennie, and D. L. Rowe, Dynamics of large-scale brain activity in normal arousal states and epileptic seizures, *Phys. Rev. E* **65**, 041924 (2002).
- [45] P. A. Robinson, C. J. Rennie, D. L. Rowe, and S. C. O'Connor, Estimation of multiscale neurophysiologic parameters by electroencephalographic means, *Hum. Brain Mapp.* **23**, 53 (2004).
- [46] P. A. Robinson, C. J. Rennie, D. L. Rowe, S. C. O'Connor, and E. Gordon, Multiscale brain modelling, *Phil. Trans. R. Soc. B* **360**, 1043 (2005).
- [47] P. A. Robinson, C. J. Rennie, D. L. Rowe, S. C. O'Connor, J. J. Wright, E. Gordon, and R. W. Whitehouse, Neurophysical modeling of brain dynamics, *Neuropsychopharmacol.* **28**, S74 (2003).
- [48] D. Rowe, P. A. Robinson, and C. J. Rennie, Estimation of neurophysiological parameters from the waking EEG using a biophysical model of brain dynamics, *J. Theor. Biol.* **231**, 413 (2004).
- [49] S. J. Van Albada, C. J. Rennie, and P. A. Robinson, Variability of model-free and model-based quantitative measures of EEG, *J. Integr. Neurosci.* **6**, 279 (2007).
- [50] P. A. Robinson, C. J. Rennie, J. J. Wright, and P. D. Bourke, Steady states and global dynamics of electrical activity in the cerebral cortex, *Phys. Rev. E* **58**, 3557 (1998).
- [51] V. K. Jirsa and H. Haken, Field Theory of Electromagnetic Brain Activity, *Phys. Rev. Lett.* **77**, 960 (1996).
- [52] P. A. Robinson, C. J. Rennie, and J. J. Wright, Propagation and stability of waves of electrical activity in the cerebral cortex, *Phys. Rev. E* **56**, 826 (1997).
- [53] S. J. Schiff, X. Huang, and J. Wu, Dynamical Evolution of Spatiotemporal Patterns in Mammalian Middle Cortex, *Phys. Rev. Lett.* **98**, 178102 (2007).
- [54] F. W. Olver, D. Lozier, R. Boisvert, and C. Clark, *NIST Handbook of Mathematical Functions* (Cambridge University, Cambridge, England, 2010).
- [55] P. C. Bressloff and J. D. Cowan, The functional geometry of local and horizontal connections in a model of V1, *J. Physiol.* **97**, 221 (2003).
- [56] J. S. Lund, A. Angelucci, and P. C. Bressloff, Anatomical substrates for functional columns in macaque monkey primary visual cortex, *Cereb. Cortex* **13**, 15 (2003).
- [57] D. R. Muir, N. M. Da Costa, C. C. Girardin, S. Naaman, D. B. Omer, E. Ruesch, A. Grinvald, and R. J. Douglas, Embedding of cortical representations by the superficial patch system, *Cereb. Cortex* **21**, 2244 (2011).

- [58] R. Malach, Y. Amir, M. Harel, and A. Grinvald, Relationship between intrinsic connections and functional architecture revealed by optical imaging and in vivo targeted biocytin injections in primate striate cortex, *Proc. Natl. Acad. Sci. USA* **90**, 10469 (1993).
- [59] L. C. Sincich and G. G. Blasdel, Oriented axon projections in primary visual cortex of the monkey, *J. Neurosci.* **21**, 4416 (2001).
- [60] W. Singer, Neuronal synchrony: A versatile code for the definition of relations? *Neuron* **24**, 49 (1999).
- [61] P. Uhlhaas, G. Pipa, B. Lima, L. Melloni, S. Neuenschwander, D. Nikolić, and W. Singer, Neural synchrony in cortical networks: History, concept and current status, *Front Integr. Neurosci.* **3**, 17 (2009).
- [62] P. A. Anderson, J. Olavarria, and R. C. Van Sluyters, The overall pattern of ocular dominance bands in cat visual cortex, *J. Neurosci.* **8**, 2183 (1988).
- [63] K. D. Miller and M. O. Stryker, The development of ocular dominance columns: Mechanisms and models, in *Connectionist Modeling and Brain Function: The Developing Interface*, edited by S. J. Hanson and C. R. Olson (MIT, Cambridge, MA, 1990).
- [64] N. V. Swindale, Role of visual experience in promoting segregation of eye dominance patches in the visual cortex of the cat, *J. Comp. Neurol.* **267**, 472 (1988).
- [65] A. K. Engel, P. R. Roelfsema, P. Fries, M. Brecht, and W. Singer, Role of the temporal domain for response selection and perceptual binding, *Cereb. Cortex* **7**, 571 (1997).